

# Hot carrier extraction with plasmonic broadband absorbers

Charlene Ng,<sup>1,2,\*</sup> Jasper Cadusch,<sup>3</sup> Svetlana Dligatch,<sup>4</sup> Ann Roberts,<sup>3</sup>  
Timothy J. Davis,<sup>3,2</sup> Paul Mulvaney,<sup>5</sup> and Daniel E. Gómez<sup>1,2,3,†</sup>

<sup>1</sup>CSIRO, Manufacturing, Private Bag 33, Clayton, VIC, 3168, Australia

<sup>2</sup>Melbourne Centre for Nanofabrication, Australian National Fabrication Facility, Clayton VIC 3168, Australia

<sup>3</sup>School of Physics, The University of Melbourne, Parkville, VIC, 3010, Australia

<sup>4</sup>CSIRO, Manufacturing, PO Box 218, Lindfield NSW 2070, Australia

<sup>5</sup>Bio21 Institute & School of Chemistry, The University of Melbourne, Parkville VIC 3010, Australia

Hot charge carrier extraction from metallic nanostructures is a very promising approach for applications in photo-catalysis, photovoltaics and photodetection. One limitation is that many metallic nanostructures support a single plasmon resonance thus restricting the light-to-charge-carrier activity to a spectral band. Here we demonstrate that a monolayer of plasmonic nanoparticles can be assembled on a multistack layered configuration to achieve broadband, near-unit light absorption, which is spatially localised on the nanoparticle layer. We show that this enhanced light absorbance leads to  $\sim 40$ -fold increases in the photon-to-electron conversion efficiency by the plasmonic nanostructures. We developed a model that successfully captures the essential physics of the plasmonic hot-electron charge generation and separation in these structures. This model also allowed us to establish that efficient hot carrier extraction is limited to spectral regions where the photons possessing energies higher than the Schottky junctions and the localised light absorption of the metal nanoparticles overlap.

Metal nanoparticles exhibit absorption cross-sections for incident light that can far exceed their physical dimensions. This strong interaction with light originates from the excitation of collective oscillations of surface charges in the nanoparticles, commonly referred to as surface plasmons. Plasmons can relax radiatively by re-emitting photons or non-radiatively creating a transient population of non-equilibrium (hot) charge-carriers<sup>1-3</sup>, which in a chemically inert environment, transfer their energy to the metal lattice resulting in nanoparticle heating<sup>4</sup>.

However, it is also possible for these hot charge carriers to be deposited into acceptor states of adsorbates<sup>5</sup> or to be transferred to an accepting medium creating charge-separated states with sufficient chemical potential energy to drive chemical (redox) reactions. For instance, in metal-semiconductor Schottky junctions, plasmon relaxation can result in the emission of hot charge carriers into the conduction band of the semiconductor<sup>6</sup>, a charge-separation process that requires photon energies below the band gap energy of the semiconductors and which has been used in photovoltaics<sup>7</sup>, photodetection<sup>8</sup> and photocatalysis<sup>9,10</sup>. Plasmonic hot charge-carrier generation has recently been used for the light-driven disso-

ciation of hydrogen<sup>11,12</sup>, oxidation of ethylene<sup>13</sup>, cross-coupling reactions<sup>14</sup>, reduction of nitro-aromatics to azo compounds<sup>15</sup> and other reactions involving more complex organic molecules<sup>16-18</sup>.

The plasmon hot-carrier relaxation pathway is a process that depends on<sup>19</sup>: (i) the efficiency of the charge transfer that must take place at relevant interfaces, (ii) the charge separation following light absorption and (iii) the absorption of incident photons. Therefore, it is expected that the rate of plasmonic hot-charge carrier relaxation can be substantially increased under conditions where the metal nanostructures absorb nearly all incident photons across a broad spectral bandwidth<sup>20,21</sup>. Typically, near unit broadband absorption has been achieved with metal-insulator-metal (MIM) structures<sup>22-25</sup>. These consist of a thin insulator or dielectric layer ( $< 100$  nm) sandwiched between a metal mirror and a thin top layer of light absorbing metal nanostructures. By replacing the insulator layer in an MIM structure with a semiconductor such as TiO<sub>2</sub>, it should be possible to extract plasmonic hot-carriers using a Schottky junction that exhibits near unit broadband absorption<sup>20</sup>. In addition to the expected increases in hot-carrier generation efficiencies, near-unit broadband absorption is an ideal model system to study the mechanism of photo-conversion in plasmonic structures.

Here we present a study on the extraction of plasmonic hot charge carriers from a monolayer of Au nanoparticles capable of absorbing up to  $> 90\%$  of incident visible light in a metal-semiconductor-metal (MSM) configuration. Examinations of the photoelectrochemical behaviour of such structures reveal significant enhancements in the yields of hot carrier extraction. Furthermore, with the aid of a simple phenomenological model, we establish that plasmon non-radiative relaxation yields uniform energy and momentum distributions of the generated charge carriers, which limit the spectral bandwidth of hot carrier extraction.

## Results

Figure 1a shows the metal-semiconductor-nanoparticle structures, which consist of an optically thick metal film and a *single layer* of Au nanoparticles, separated by a thin TiO<sub>2</sub> layer. These samples were made by means of sequential physical vapour deposition of materials (see Methods section), a large scale method resulting in a densely-packed monolayer of Au nanoparticles [shown in the scanning electron microscope (SEM)

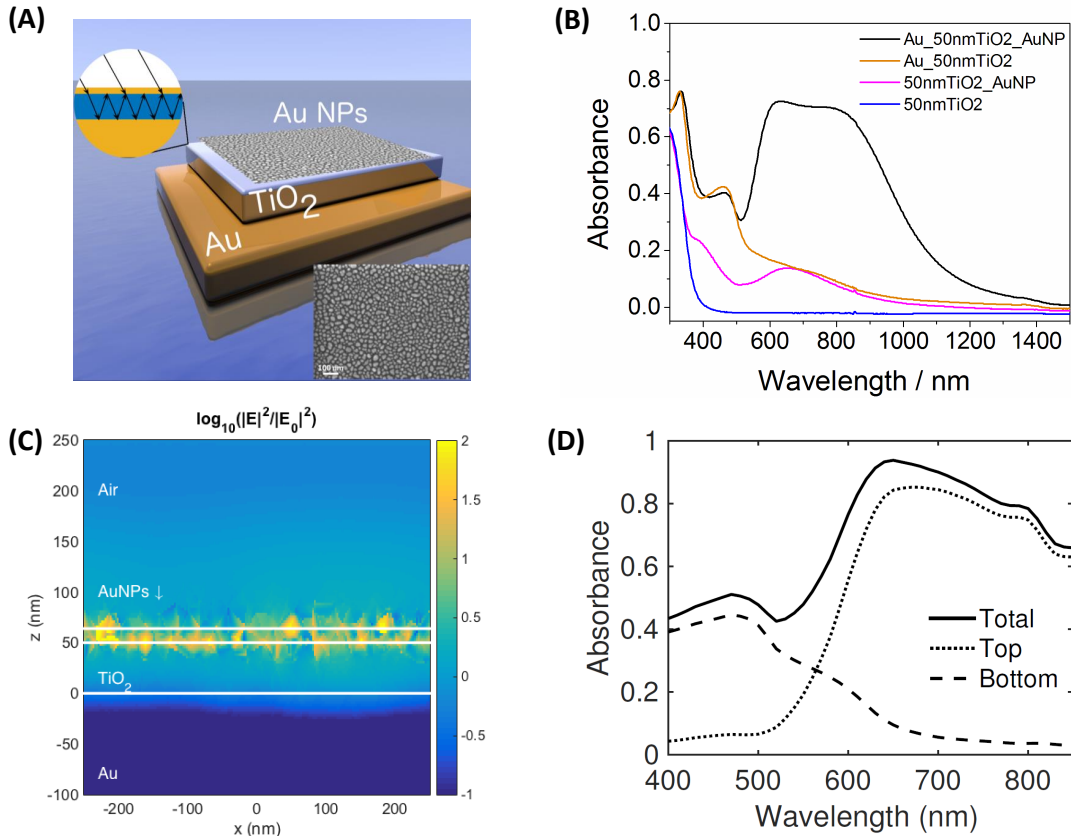


FIG. 1: **Architecture and working principle of plasmonic broadband absorber structure.** (A) Schematic of the broadband absorber structure with  $\text{TiO}_2$  positioned in between the Au mirror and Au nanoparticles. Inset: multiple internal reflection and interference interpretation of unit absorption<sup>26</sup>. Also shown is an SEM of the Au nanoparticle monolayer. (B) Absorbance spectra of Au\_50nmTiO2\_AuNP, Au\_50nmTiO2 (without Au NPs), 50nmTiO2\_AuNP (without mirror) and bare  $\text{TiO}_2$ . These spectra were calculated as  $A = 1 - R - T$ , where  $R$  and  $T$  are the measured Reflectance and Transmission spectra (diffuse + specular). (C) Spatial distribution of the Electric field of the metal–semiconductor–nanoparticle structures at 650 nm. The values are shown on a logarithmic scale of the absolute magnitude square of the electric field relative to the incident field. (D) Plot of the absorption of incident light *vs.* wavelength for the top and bottom metal layers.

image of Figure 2a: 10 nm thick, average diameter of 20 nm, dimensions that are  $\leq$  mean-free path for hot electrons in Au<sup>27</sup>. Size histogram in Supplementary figure S1]. This nanoparticle ensemble, when deposited on top of glass-supported  $\text{TiO}_2$  films, exhibits a single-band absorption centred around 620 nm (with 0.15 absorbance) characteristic of localised surface plasmon resonances of Au nanoparticles on materials with a high refractive index<sup>10</sup>. On the contrary, the metal–semiconductor–nanoparticle structure (Au\_50nmTiO2\_AuNP) exhibits a distinctively broadband absorption in a spectral region ranging from 600 nm to 1000 nm, reaching absorbance values of up to  $\sim 0.75$ : a 5-fold increase in absorbance, when compared to the control sample without the reflecting layer (50nmTiO2\_AuNP). These absorption spectra were calculated as  $A = 1 - R - T$ , where  $R$  and  $T$  correspond to measured reflectance and transmission spectra (both their diffuse and specular components, see

Methods section).

In the metal–semiconductor–nanoparticle structures, the thickness of the  $\text{TiO}_2$  layer was chosen, with the aid of numerical solutions of Maxwell equations (see supporting information section S1) such that the structure exhibited low reflection ( $R$ ) of light in the visible. Given that the thickness of the supporting metal layer is much greater than the skin depth of the metal, there is no transmission of light in these structures ( $T = 0$ ) and conservation of energy dictates that the absorbance  $A$  is therefore given by  $A = 1 - R$ , implying that (near) unit absorption occurs when  $R$  (tends to) equals zero.

Near–unit absorption in these structures originates from optical destructive interference between directly reflected light and the multiple reflections taking place at the other interfaces of the multi–layer stack<sup>26</sup> (see diagram of figure 1A). Other interpretations assign the near–unit absorption of light to a renormalization of the po-

larizability of the nanoparticles due to their interactions with the mirror<sup>28</sup> or to optical impedance matching between the structure and free space, a phenomenon that occurs due to a magnetic response that arises from anti-parallel currents taking place on both the metal mirror and the nanoparticles<sup>22–25</sup>. According to the numerical simulations shown in Figure 1C, at a wavelength of 650 nm there is a strong (and sub-wavelength) localisation of the electric field at the spatial location of the metal nanoparticles, which accounts for the high absorbance reported in Figure 1B. As a function of the incident photon wavelength, Figure 1D shows that the spatial location of the absorption occurs at the nanoparticle monolayer for long wavelengths, but it becomes localised on the metal mirror at shorter wavelengths.

**Photo-currents.** Subsequent to light absorption, non-radiative relaxation of nanoparticle plasmons can result in the transfer of the incident photon energy to a hot electron, which can obtain sufficient energy and momentum to overcome the Schottky barrier existent at the Au nanoparticle–TiO<sub>2</sub> interface<sup>29</sup>. To measure this possible photon-to-electron conversion, we employed the metal–semiconductor–nanoparticle structures as photoanodes in photo-electrochemical cells, as illustrated in the diagram of figure 2A<sup>30–32</sup>. Electron injection from the metal nanoparticles into accepting states (such as the conduction band or trap states) of the TiO<sub>2</sub> film, leaves a positive charge (hole) on the Au nanoparticles which can be neutralised by electron donating species in solution. Injected electrons in the TiO<sub>2</sub> can then be collected by the mirror (which also acts as an electrical contact) and transported to a Pt counter electrode, where reduction reactions take place. The overall process results in the generation of measurable photocurrents.

Figure 2B shows the measured photocurrents for three photoanodes: (i) metal–semiconductor–nanoparticle (Au\_50nmTiO<sub>2</sub>\_AuNP), (ii) metal-supported TiO<sub>2</sub> thin film (Au\_50nmTiO<sub>2</sub>), and (iii) a semiconductor–supported Au nanoparticle monolayer (50nmTiO<sub>2</sub>\_AuNP). These measurements were performed under visible light irradiation (495 nm long pass filter) in a two-electrode configuration with an applied potential of 0.5 V, and under conditions where the electrolyte consisted of aqueous 0.5 M Na<sub>2</sub>SO<sub>4</sub> with 20 v/v% methanol (purged with N<sub>2</sub>, more details can be found in the methods section).

The long-pass filter eliminates possible direct excitation of electron–hole pairs in TiO<sub>2</sub> with photon energies above its band gap (see Supplementary figure S2 where we estimate the band-gap of the TiO<sub>2</sub>). Indeed, significant photocurrents at wavelengths higher than 495 nm were only observed when Au nanoparticles were present on the electrodes. The photocurrents observed in figure 2B can only be a consequence of the excitation and extraction of hot charge-carriers from the Au nanoparticles into the Pt counter electrode. These photocurrents were detected only when the visible light was turned on and the currents returned to the background in the

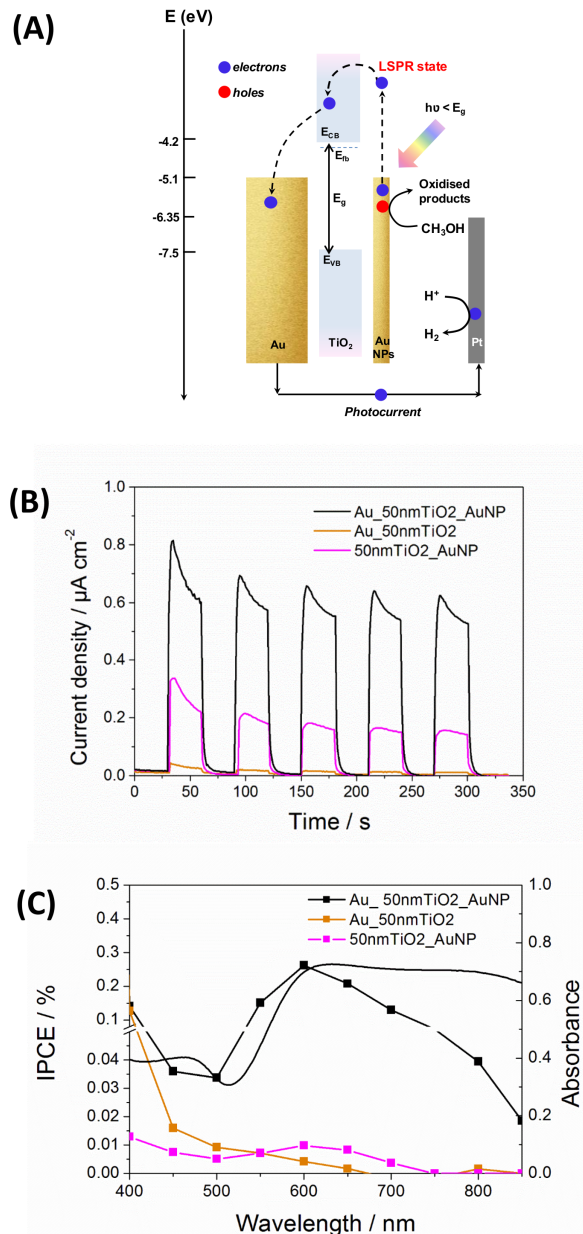


FIG. 2: **Photoelectrochemical and absorption performance of the plasmonic broadband absorber structure.** (A) Illustration of the working principle: Upon visible light illumination and plasmon non-radiative relaxation, hot electrons in the Au nanoparticles can be injected to TiO<sub>2</sub> and be transported subsequently to the Pt counter electrode and measured as photocurrents.  $E_{CB}$ ,  $E_{VB}$  and  $E_g$  refer to conduction band, valence band and band gap energy of TiO<sub>2</sub> respectively. (B) Photocurrent generation under both visible light illumination ( $\geq 495$  nm cut-off filter) and in the dark in a 2 electrode system vs Pt wire; applied voltage of 0.5 V and 0.5 M Na<sub>2</sub>SO<sub>4</sub> + 20 v/v% methanol electrolyte solution. (C) IPCE values of Au\_50nmTiO<sub>2</sub>\_AuNP, Au\_50nmTiO<sub>2</sub> and 50nmTiO<sub>2</sub>\_AuNP and absorbance data of Au\_50nmTiO<sub>2</sub>\_AuNP. Also shown is the absorbance spectrum of the metal–semiconductor–nanoparticle structure.

dark. This confirms that the measured electrical currents were photo-induced, as opposed to dark (thermal) currents enhanced by the applied bias voltage [see figure S4 where the effect of the applied bias on the measured photocurrents is reported]. The measurements were reproducible and stable for all of the samples, indicating the absence of irreversible electrochemical damage to the photoanodes. The anodic currents measured with the metal–semiconductor–nanoparticle sample ( $0.56 \mu\text{A cm}^{-2}$ ) were 3.5 times larger than those obtained with the semiconductor–supported Au nanoparticle monolayer ( $0.16 \mu\text{A cm}^{-2}$ ) electrode. The magnitude of these photocurrents increased linearly with the incident illumination power and illumination leads to a change in the measured photovoltage (see Supplementary figures S3 and S5).

**Incident photon to electron conversion efficiency (IPCE).** The IPCE as a function of wavelength was measured for all three samples, and the results are shown in figure 2C. The metal–supported  $\text{TiO}_2$  thin film (Au\_50nmTiO2) did not lead to an appreciable IPCE even though it showed a relatively high absorption at 460 nm. On the contrary, the non-vanishing IPCE spectrum measured for the semiconductor–supported Au nanoparticle monolayer (50nmTiO2\_AuNP) closely follows the lineshape of its corresponding optical absorption spectrum shown in figure 1B, indicating a strong correlation with the photoexcitation of localised surface plasmon resonances. For the metal–semiconductor–nanoparticle photo-anode (Au\_50nmTiO2\_AuNP), the measured IPCE has a broadband character with a maximum of 0.27 % at around 600 nm, an efficiency  $\sim 20$  times larger than the one measured for the semiconductor–supported Au nanoparticle monolayer (50nmTiO2\_AuNP).

Further increases in the absorbance and (consequently) IPCE values of the metal–semiconductor–nanoparticle structures can be achieved by decreasing the thickness of the  $\text{TiO}_2$  layer from 50 nm to 30 nm, which as shown in figure 3(A), leads to an absorbance of up to  $\geq 95\%$  (maximum of 99% at 544 nm). The IPCE in turn increases by about a factor of  $4\times$  for wavelengths below 600 nm, but remains almost unchanged at longer wavelengths. In figure 3(B), we show that when the mirror is modified from Au to Al in the metal–semiconductor–nanoparticle stacks (at fixed semiconductor thickness), the measured light absorption increases to  $\geq 80\%$  (and reaches a maximum of 87% at 590 nm) with concomitant increases in IPCE values. Figure 3(C) depicts a summary of the IPCE enhancements attainable with the metal–semiconductor–nanoparticle structures investigated, which shows increases of almost  $40\times$  with respect to the semiconductor–supported Au nanoparticle monolayer.

The measured IPCE spectral lineshapes for the metal–semiconductor–nanoparticle samples track the corresponding optical absorption spectra for wavelengths shorter than  $\sim 700$  nm, but exhibit a characteristic rapid

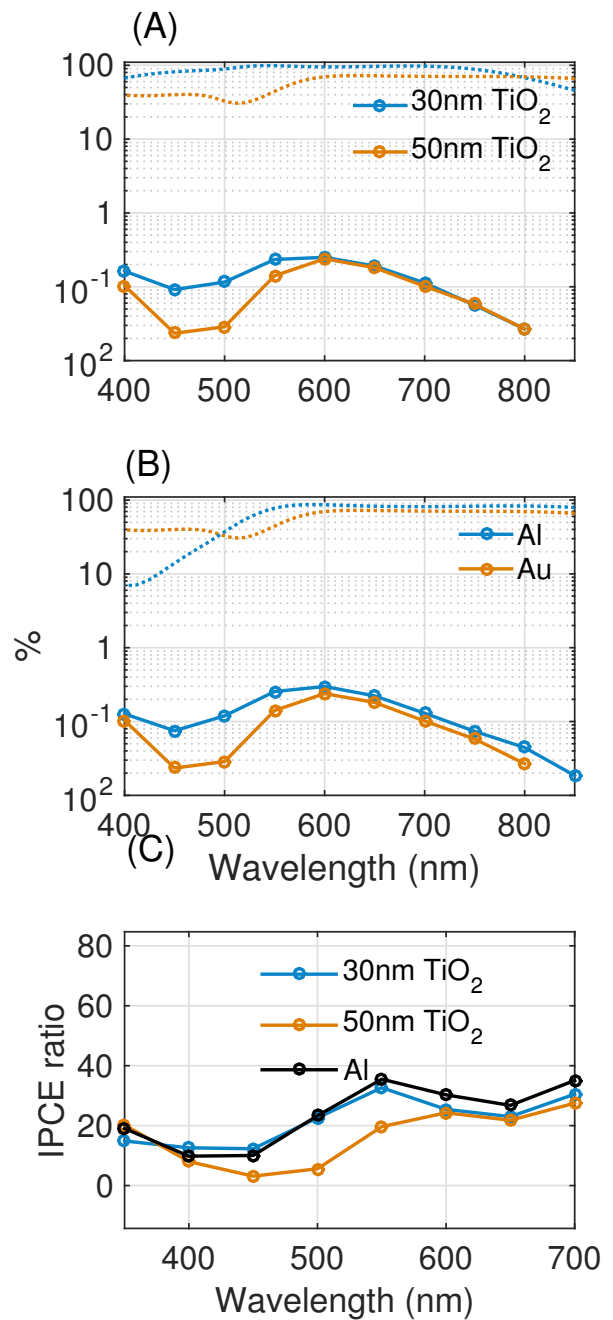


FIG. 3: **Effect of structural parameters on measured IPCE.** (A)  $\text{TiO}_2$  thickness. Dashed lines are the measured optical absorption spectra of samples (obtained from diffuse reflectance measurements) with 30 nm and 50 nm of  $\text{TiO}_2$ . Dotted lines show the corresponding IPCE values. (B) Work function of the reflector. Measured absorption spectra for samples where the metal reflector was made of Au or Al and their corresponding IPCE spectra (dotted lines). The thickness of  $\text{TiO}_2$  was kept fixed at 50 nm. (C) Ratio of measured IPCE relative to the results obtained for the  $\text{TiO}_2$  supported Au nanoparticle monolayer.

decay at longer wavelengths (in spite of measured strong absorbance) which occurs as a consequence of the mechanism of hot-charge carrier extraction that we proceed to discuss next.

### Discussion

The IPCE at a specific wavelength  $\lambda$  is proportional to the photon absorption efficiency of the metal nanoparticles  $A_{layer}$  and the probability  $\eta$  that the absorbed photon results in a collected electron in the photoelectrochemical circuit<sup>27</sup>:

$$\text{IPCE}(\lambda) = A_{layer}(\lambda) \times \eta(\lambda). \quad (1)$$

The former can be determined by solving Maxwell's equations for the structures, which also provide information on, for instance, the spectral and spatial location of the light-absorption events (e.g. figure 1D).  $A_{layer}$  is optimal for structures that exhibit unit absorption of light at the position of the nanoparticle monolayer (i.e.  $A_{layer} = 1$ ).

In order to get a quantitative estimate for  $\eta$ , as a first-order approximation, this parameter can be expressed as (more details in Supplementary section S3):

$$\eta = \eta_{inj} \times \eta_{trpt} \times \eta_{injm} \times \eta_{ed}, \quad (2)$$

which conceptually results from the following sequence of events (see the diagram shown in figure 2): (i) the injection of a plasmon-derived hot electron across the nanoparticle-semiconductor Schottky barrier, with probability  $\eta_{inj}$ , (ii) elastic transport of the injected electrons across the semiconductor layer with an associated probability  $\eta_{trpt}$ , (iii) the injection of the charge carrier into the metal reflector, occurring with a probability  $\eta_{injm}$ . An additional assumption is made in that once injected into the reflector, the charge carrier will travel through an external circuit to the counter electrode where finally (iv) the total current is measured when an electron-donating species in solution injects an electron into the positively-charged metal nanoparticles with a probability  $\eta_{ed}$ <sup>19</sup>.

The hot-electron injection efficiency  $\eta_{inj}$  is determined by the energy-momentum distribution of the hot-electron population that results from Landau damping of plasmons. Little is known at present about these energy-momentum distributions. To get an estimate of  $\eta_{inj}$ , we assume that Landau damping produces an isotropic momentum distribution<sup>4</sup> and approximate the energy distribution of hot-electrons as a product of the initial and final (parabolic) density of electron states in the metal. We furthermore consider the initial states to have energies ranging from below (and up to) the Fermi level  $E_F$ , whereas the final states are thought to have energies from the Fermi level and up to  $E_F +$  the incident photon energy<sup>3</sup>.  $\eta_{inj}$  is then approximated as  $P(E_e > \Phi_{SB}|k_e) \otimes \langle T \rangle$  [see equation (S10)], where:  $\langle T \rangle$  is the transmission coefficient for electrons across the metal nanoparticle-semiconductor interface (calculated taking into account conservation of momentum, see section S3.1c) and,  $P(E_e > \Phi_{SB}|k_e)$  is the fraction of the hot-electron population for which the electrons

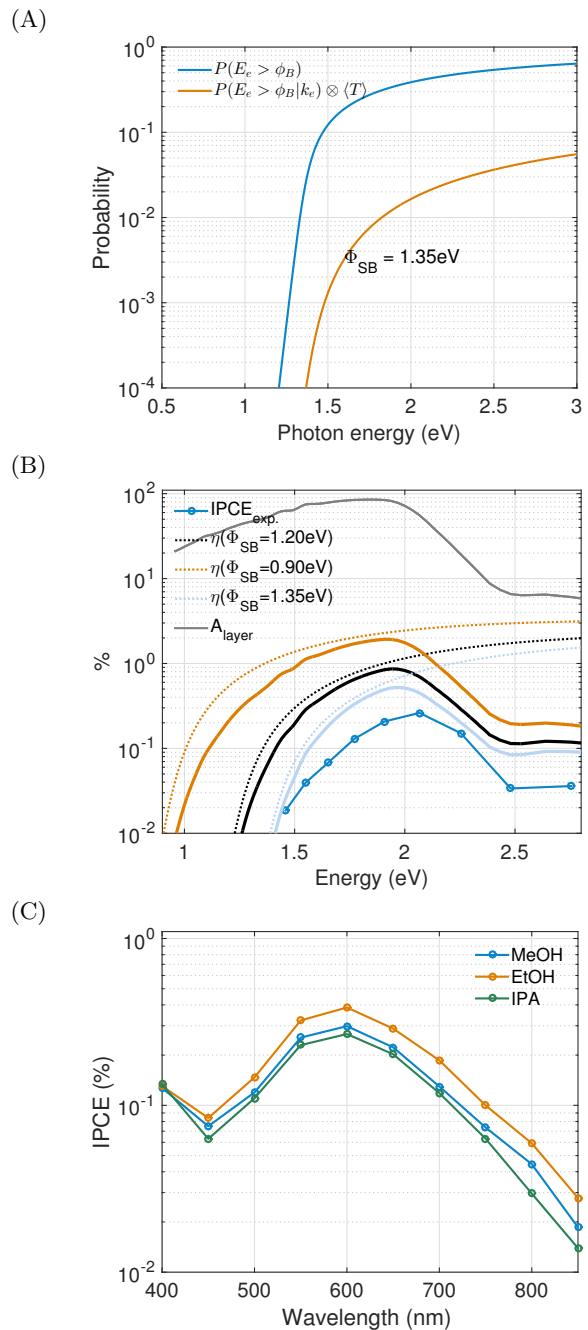


FIG. 4: **Estimate of the efficiency.** (A) hot-electron injection probability  $\eta_{inj} = P(E_e > \Phi_{SB}|k_e) \otimes \langle T \rangle$ .  $P(E_e > \Phi_{SB}|k_e)$  is the joint probability that plasmonic hot-electrons have energies  $E_e$  in excess of the Schottky barrier  $\Phi_{SB}$  and a momentum  $k_e$  with a component perpendicular to the metal-semiconductor interface that lies within the escape cone.  $\langle T \rangle$  is the electron transmission coefficient at the nanoparticle-TiO<sub>2</sub> interface. Also shown for comparison, is the probability  $P(E_e > \Phi_{SB})$  that the plasmon-derived hot-electrons have energies  $E_e$  in excess of  $\Phi_{SB}$ . (B)  $\eta$ : absorbed photon-to-electron conversion efficiency. It shown in this figure for two values of  $\Phi_{SB}$ . The solid curves represent the theoretical estimate of the efficiency given by  $A_{layer} \times \eta$ , where  $A_{layer}$  (dashed grey line) is the calculated absorption at the nanoparticle layer. The modelled and measured IPCE ( $\text{IPCE}_{exp}$ ) show similar lineshapes exhibiting a pronounced decrease as the wavelength of incident photons approaches  $\Phi_{SB}$ , consistent with the data shown in (A). In these calculations values of 0.96 eV<sup>33</sup>, 1.20 eV<sup>34</sup> and 1.35 eV were used for  $\Phi_{SB}$ . (C) Measured IPCE spectra for cases with Methanol (MeOH), Ethanol (EtOH) and Isopropanol (IPA) as the sacrificial electron donors in solution.

have a momentum  $k_e$  that lies within the escape cone of the metal–semiconductor interface and with energies  $E_e$  above the Schottky barrier [see equation (S5)]. As shown in figure 3A,  $\eta_{inj}$  increases slowly with incident photon energy [details of the calculations leading to figure 4(A) are shown in the supplementary section S3, note that we do not consider possible quantum mechanical tunnelling of electrons under the barrier].

The charge–carrier transport efficiency  $\eta_{trpt}$  is the probability that, after injection, the charge carrier is transported through the  $\text{TiO}_2$  layer, without experiencing scattering and/or trapping at defect states, the probability of which we assume to be determined by the ratio of the thickness of the metal–oxide layer and the mean–free path for electrons<sup>9</sup> (see section S3.2).  $\eta_{inj,m}$ , is approximated by the transmission coefficient for electrons to traverse the semiconductor–metal (reflector) interface, thus accounting for possible reflections due to the momentum and energy mismatch (more details in section S3.3). For simplicity, we do not account for possible electron flow from the metal reflector into the semiconductor, which may originate from the excitation and decay of surface plasmon polaritons at the metal/semiconductor interface. This charge flow will have an opposite direction and thus decrease the measured photocurrents and IPCE<sup>6,11</sup>.

The calculated values of  $\eta$  (assuming  $\eta_{ed} = 1$ ) and  $A_{layer} \times \eta$  produce the dotted and continuous lines in Figure 4B respectively.  $\eta$  is strongly dependent on the magnitude of  $\Phi_{SB}$ , the thickness of the oxide layer and the height of the energy barrier preventing electron injection at the semiconductor–mirror interface. The model satisfactorily reproduces the slow increase of the measured IPCE with incident photon energy, in particular, for a value of  $\Phi_{SB} = 1.20$  eV reported by the experiments of Lee *et al*<sup>40</sup>. In the model, this curvature originates from a combination of two factors: (i) the almost rectangular shape of the energy distribution of hot carriers, which limits the number of these carriers that meets the energy requirements for injection [i.e.  $E > \Phi_{SB}$ , see curve  $P(E_e > \Phi_{SB})$  of fig. 4A] and, (ii) the narrow escape cone for carriers from the metal nanoparticles and into the semiconductor, which severely limits the total fraction of “useful” charge carriers by almost 75% [see figure S9(B)]. Factor (i) is a consequence of the assumed broad energy distribution of initial states, whereas (ii) originates from the assumed uniform distribution of electron momenta resulting from Landau damping. At higher energies, the calculated drop in  $A_{layer} \times \eta$  is in qualitative agreement with the experimental results, which is a consequence of the fact that at these wavelengths, light is predominantly absorbed by the mirror (see figure 1D). A simple conclusion that can be drawn from these observations is that, in spite of the spectrally broad and strong absorption of light achievable with the metal–semiconductor–nanoparticle structure, the generation of charge–carriers from plasmon relaxation in this architecture is limited to those spectral regions where the incident photon ener-

gies are in excess of the metal–semiconductor Schottky barrier and below the onset for strong absorption by the metal reflecting layer.

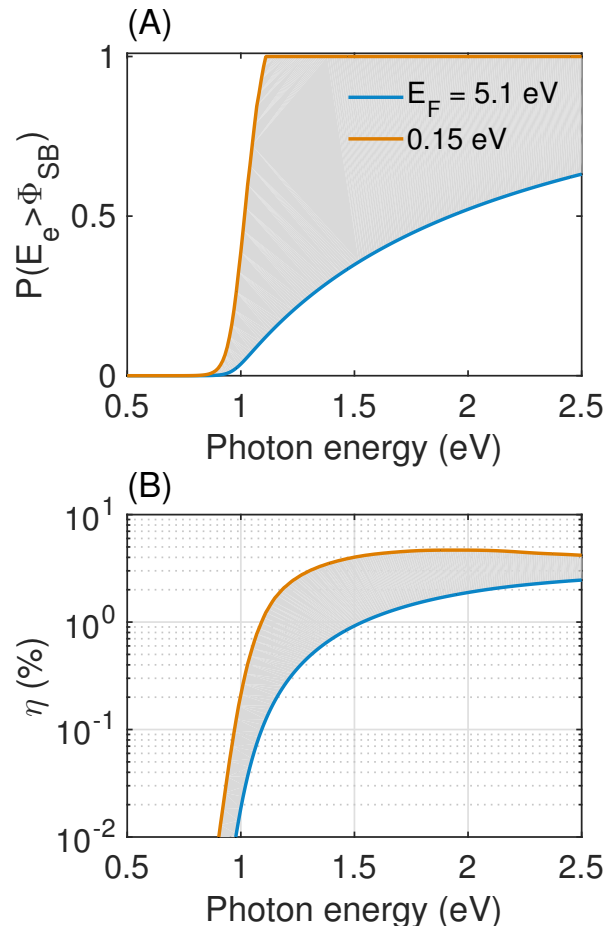


FIG. 5: **Narrow distribution of states near the Fermi level of the metal.** (A) Distribution of electron energies and (B) calculated internal quantum efficiency. The shaded areas highlight the attainable differences.  $\Phi_{SB} = 0.98$  eV.

According to the model, the ICPE is expected to increase if the plasmon relaxation were to result in narrow electron energy distributions. This is a situation that can be modelled by considering that the bottom of the conduction band is close ( $\sim 0.15$  eV) to the Fermi level of the metal<sup>3,41</sup>, a hypothetical (and somewhat unrealistic) situation depicted in figure 5. The orange curve in fig. 5(A) shows that for this hypothetical case, the fraction of the population of hot–electrons with  $E_e > \Phi_{SB}$  is almost a step function of the incident photon energy and becomes energy–independent (and unit) for energies slightly above  $\Phi_{SB}$ . This step–like  $P(E_e > \Phi_{SB})$  drastically changes the shape of  $\eta$  [fig. 5(B)] and leads to an overall increase in the expected internal efficiency

The measured IPCEs are well below the predictions of our model, which were made under the assumption of unit  $\eta_{ed}$ .  $\eta_{ed}$  in the photo–electrochemical configuration that we adopted for extracting hot–charge carriers

is expected to be limited by the kinetics of charge and mass transfer occurring at the solid–liquid interfaces. In figure 4C we show the measured IPCE changes for a sample where the (sacrificial) electron donating species were changed from Methanol (MeOH) to Ethanol (EtOH) and to Isopropanol (IPA). An uniform increase in the IPCE is clearly observable for the case of EtOH, which is attributable solely to changes in the kinetic and thermodynamic processes taking place at the photoanode/liquid junction.  $\eta_{ed}$  is a parameter which is not included in our theoretical description of plasmonic hot–charge carrier extraction, but which seems to play a key role in determining the IPCE in our photo–electrochemical cell, an observation also conjectured in (solid state) plasmonic solar cells<sup>42</sup>, where it was found that hole accumulation at the metal nanoparticles limits device performance.

In summary, we have demonstrated the extraction of plasmonic–derived charge carriers from a multi–layer stack comprising a monolayer of Au nanoparticles. These multilayer structures exhibit broadband and intense absorption of light, which leads to a significant increase in the incident photon–to–electron conversion efficiencies. We have developed a simple model to describe the hot–charge carrier generation and transport in this system, which satisfactorily describes the measured IPCE spectra. According to this model, the broad distribution of hot–charge carrier energies and their uniform distribution of momenta, account for the weak increase in measured IPCE with incident photon energies. A more efficient strategy for generating and extracting plasmonic hot charge carriers is one that combines strong near–unit absorption of light with a mechanism, such as the plasmon–induced metal–to–semiconductor interfacial charge transfer transition, where a quantum yield for electron injection of >24% has been found to be independent of the incident photon energy<sup>43</sup>. Our results demonstrate that significant enhancements in the efficiencies of opto–electronic and photoelectrochemical devices that operate with plasmonic–derived hot–charge carriers can be achieved by tailoring the optical properties of the plasmonic nanostructures.

## Methods

**Material fabrication and Characterization** The Al and Au mirrors were deposited onto glass substrates with an in–house constructed electron beam evaporator equipped with transmittance monitoring. A thin layer of Cr was deposited prior to the Au deposition to ensure good adhesion to the glass substrate. For both Al and Au mirrors, deposition was conducted by monitoring the optical transmittance to ensure the films had no transmittance of light. Subsequently, the TiO<sub>2</sub> layers (30 nm and 50 nm) were deposited onto the metal supporting mirrors through an ion–assisted electron beam evaporation process at 200°C. The bombardment of oxygen during the deposition process ensured the deposition of stoichiometric TiO<sub>2</sub> onto the mirrors. Lastly, the Au nanoparticles were deposited with a similar electron beam evaporation process with two types of in–situ optical monitoring. A broadband transmittance was utilized to monitor the absorption of the Au nanoparticles, while an ellipsometry measurement at 633 nm was employed to achieve non–overlapping particles and detect the deposition point at which the particles coagulate to form continuous films. Scanning electron microscope (SEM) images of the Au NPs were obtained with a Zeiss Merlin Field Emission Scanning Electron

Microscope. The diffuse and specular reflectance ( $R$ ) and transmittance ( $T$ ) spectra were measured using a UV–VIS spectrophotometer (Perkin–Elmer Lambda 1050) with an integrating sphere and small spot kit. With these two measurements, the absorbance was calculated as  $A = 1 - R - T$ .

**Photoelectrochemical measurements** The designed structure and platinum wire was employed as the working electrode and counter electrode respectively in a 2 electrode system. The exposed surface area of the working electrode was 1 cm in diameter. The electrolyte solution used was 0.5 M Na<sub>2</sub>SO<sub>4</sub> (anhydrous, Sigma–Aldrich, ≥99%) with 20 v/v % amount of methanol (Sigma–Aldrich, ≥99.9%) or ethanol (Sigma–Aldrich, ≥99.9%) as the sacrificial reagent. The 0.5 M Na<sub>2</sub>SO<sub>4</sub> was employed to reduce the resistance in the electrolyte solution. Prior to the photocurrent measurements, the solutions were purged with N<sub>2</sub> gas to remove electron scavenging O<sub>2</sub>. The working potential was set at +0.5 V versus the Pt wire and the devices were illuminated with light from a 300 W Xenon lamp (Newport Model no. 669092) using a ≥ 495 nm cut–off filter (Thorlabs FGL–495). The applied voltage and photocurrent  $I$  were recorded with a potentiostat (AutoLab PGSTAT204). To measure the IPCE values, light from the Xenon lamp was coupled to a monochromator with a bandwidth of 5 nm at full width at half maximum (FWHM). The light intensity  $P$  of the monochromatic light at each wavelength was measured using a Thorlabs optical power and energy meter (Model. PM100D). The incident photon to electron efficiency (IPCE) was calculated by the following formula:

$$\text{IPCE} = 100 \times \frac{I(A/cm^2)}{P(W/cm^2)} \times \frac{1240}{\lambda(nm)}.$$

- \* Electronic address: charlene.ng@csiro.au  
 † Electronic address: daniel.gomez@csiro.au
- <sup>1</sup> Clavero, C. “Plasmon-induced hot-electron generation at nanoparticle/metal-oxide interfaces for photovoltaic and photocatalytic devices,”. *Nat Photon* **8**(2), 95–103 02 (2014).
  - <sup>2</sup> Brongersma, M. L., Halas, N. J., and Nordlander, P. “Plasmon-induced hot carrier science and technology,”. *Nat Nano* **10**(1), 25–34 01 (2015).
  - <sup>3</sup> Linic, S., Christopher, P., and Ingram, D. B. “Plasmonic-metal nanostructures for efficient conversion of solar to chemical energy,”. *Nat Mater* **10**(12), 911–921 12 (2011).
  - <sup>4</sup> Hartland, G. V. “Optical studies of dynamics in noble metal nanostructures,”. *Chemical Reviews* **111**(6), 3858–3887 06 (2011).
  - <sup>5</sup> Kale, M. J., Avanesian, T., and Christopher, P. “Direct photocatalysis by plasmonic nanostructures,”. *ACS Catalysis* **4**(1), 116–128 (2014).
  - <sup>6</sup> Furube, A., Du, L., Hara, K., Katoh, R., and Tachiya, M. “Ultrafast plasmon-induced electron transfer from gold nanodots into TiO<sub>2</sub> nanoparticles,”. *Journal of the American Chemical Society* **129**(48), 14852–14853 (2007).
  - <sup>7</sup> Mubeen, S., Lee, J., Lee, W.-r., Singh, N., Stucky, G. D., and Moskovits, M. “On the plasmonic photovoltaic,”. *ACS Nano* **8**(6), 6066–6073 (2014). PMID: 24861280.
  - <sup>8</sup> Knight, M. W., Sobhani, H., Nordlander, P., and Halas, N. J. “Photodetection with active optical antennas,”. *Science* **332**(6030), 702–704 (2011).
  - <sup>9</sup> Nishijima, Y., Ueno, K., Kotake, Y., Murakoshi, K., Inoue, H., and Misawa, H. “Near-infrared plasmon-assisted water oxidation,”. *The Journal of Physical Chemistry Letters* **3**(10), 1248–1252 (2012).
  - <sup>10</sup> Tian, Y. and Tatsuma, T. “Mechanisms and applications of plasmon-induced charge separation at TiO<sub>2</sub> films loaded with gold nanoparticles,”. *Journal of the American Chemical Society* **127**(20), 7632–7637 (2005).
  - <sup>11</sup> Mukherjee, S., Libisch, F., Large, N., Neumann, O., Brown, L. V., Cheng, J., Lassiter, J. B., Carter, E. A., Nordlander, P., and Halas, N. J. “Hot electrons do the impossible: Plasmon-induced dissociation of H<sub>2</sub> on Au,”. *Nano Letters* **13**(1), 240–247 (2013).
  - <sup>12</sup> Mukherjee, S., Zhou, L., Goodman, A. M., Large, N., Ayala-Orozco, C., Zhang, Y., Nordlander, P., and Halas, N. J. “Hot-electron-induced dissociation of H<sub>2</sub> on gold nanoparticles supported on SiO<sub>2</sub>,”. *Journal of the American Chemical Society* **136**(1), 64–67 (2014).
  - <sup>13</sup> Christopher, P., Xin, H., and Linic, S. “Visible-light-enhanced catalytic oxidation reactions on plasmonic silver nanostructures,”. *Nat Chem* **3**(6), 467–472 06 (2011).
  - <sup>14</sup> Xiao, Q., Sarina, S., Bo, A., Jia, J., Liu, H., Arnold, D. P., Huang, Y., Wu, H., and Zhu, H. “Visible light-driven cross-coupling reactions at lower temperatures using a photocatalyst of palladium and gold alloy nanoparticles,”. *ACS Catalysis* **4**(6), 1725–1734 (2014).
  - <sup>15</sup> Ke, X., Zhang, X., Zhao, J., Sarina, S., Barry, J., and Zhu, H. “Selective reductions using visible light photocatalysts of supported gold nanoparticles,”. *Green Chem.* **15**, 236–244 (2013).
  - <sup>16</sup> Wang, C. and Astruc, D. “Nanogold plasmonic photocatalysis for organic synthesis and clean energy conversion,”. *Chem. Soc. Rev.* **43**, 7188–7216 (2014).
  - <sup>17</sup> Scaiano, J. C. and Stamplecoskie, K. “Can surface plasmon fields provide a new way to photosensitize organic photoreactions? from designer nanoparticles to custom applications,”. *The Journal of Physical Chemistry Letters* **4**(7), 1177–1187 (2013).
  - <sup>18</sup> Xiao, M., Jiang, R., Wang, F., Fang, C., Wang, J., and Yu, J. C. “Plasmon-enhanced chemical reactions,”. *J. Mater. Chem. A* **1**, 5790–5805 (2013).
  - <sup>19</sup> Moskovits, M. “The case for plasmon-derived hot carrier devices,”. *Nat Nano* **10**(1), 6–8 01 (2015).
  - <sup>20</sup> Fang, Y., Jiao, Y., Xiong, K., Ogier, R., Yang, Z., Gao, S., Dahlin, A., and Käll, M. “Plasmon enhanced internal photoemission in antenna-spacer-mirror based Au/TiO<sub>2</sub> nanostructures,”. *Nano Letters* (2015).
  - <sup>21</sup> Robotjazi, H., Bahauddin, S. M., Doiron, C., and Thomann, I. “Direct plasmon-driven photoelectrocatalysis,”. *Nano Letters* (2015).
  - <sup>22</sup> Liu, Z., Liu, X., Huang, S., Pan, P., Chen, J., Liu, G., and Gu, G. “Automatically acquired broadband plasmonic-metamaterial black absorber during the metallic film-formation,”. *ACS Applied Materials & Interfaces* **7**(8), 4962–4968 (2015). PMID: 25679790.
  - <sup>23</sup> Aydin, K., Ferry, V. E., Briggs, R. M., and Atwater, H. A. “Broadband polarization-independent resonant light absorption using ultrathin plasmonic super absorbers,”. *Nat Commun* **2**, 517 11 (2011).
  - <sup>24</sup> Hedayati, M. K., Javaherirahim, M., Mozooni, B., Abdelaziz, R., Tavassolizadeh, A., Chakravadhanula, V. S. K., Zaporjtchenko, V., Strunkus, T., Faupel, F., and Elbahri, M. “Design of a perfect black absorber at visible frequencies using plasmonic metamaterials,”. *Advanced Materials* **23**(45), 5410–5414 (2011).
  - <sup>25</sup> Landy, N. I., Sajuyigbe, S., Mock, J. J., Smith, D. R., and Padilla, W. J. “Perfect metamaterial absorber,”. *Phys. Rev. Lett.* **100**, 207402 May (2008).
  - <sup>26</sup> Chen, H.-T. “Interference theory of metamaterial perfect absorbers,”. *Opt. Express* **20**(7), 7165–7172 Mar (2012).
  - <sup>27</sup> McFarland, E. W. and Tang, J. “A photovoltaic device structure based on internal electron emission,”. *Nature* **421**(6923), 616–618 02 (2003).
  - <sup>28</sup> Kwadrin, A., Osorio-A., C. I., and Koenderink, F. “Back-action in metasurface etalons,”. *arXiv:1505.02727* (2015).
  - <sup>29</sup> Mubeen, S., Hernandez-Sosa, G., Moses, D., Lee, J., and Moskovits, M. “Plasmonic photosensitization of a wide band gap semiconductor: Converting plasmons to charge carriers,”. *Nano Letters* **11**(12), 5548–5552 (2011).
  - <sup>30</sup> Thomann, I., Pinaud, B. A., Chen, Z., Clemens, B. M., Jaramillo, T. F., and Brongersma, M. L. “Plasmon enhanced solar-to-fuel energy conversion,”. *Nano Letters* **11**(8), 3440–3446 (2011).
  - <sup>31</sup> Tian, Y. and Tatsuma, T. “Plasmon-induced photoelectrochemistry at metal nanoparticles supported on nanoporous TiO<sub>2</sub>,”. *Chem. Commun.* , 1810–1811 (2004).
  - <sup>32</sup> García de Arquer, F. P., Mihi, A., Kufer, D., and Konstantatos, G. “Photoelectric energy conversion of plasmon-generated hot carriers in metal-insulator-semiconductor structures,”. *ACS Nano* **7**(4), 3581–3588 (2013). PMID: 23495769.
  - <sup>33</sup> Zhang, X., Chen, Y. L., Liu, R.-S., and Tsai, D. P. “Plasmonic photocatalysis,”. *Reports on Progress in Physics* **76**(4), 046401 (2013).

- <sup>34</sup> Lee, H., Keun Lee, Y., Nghia Van, T., and Young Park, J. “Nanoscale schottky behavior of Au islands on TiO<sub>2</sub> probed with conductive atomic force microscopy,”. *Applied Physics Letters* **103**(17), – (2013).
- <sup>35</sup> Scales, C. and Berini, P. “Thin-film schottky barrier photodetector models,”. *Quantum Electronics, IEEE Journal of* **46**(5), 633–643 May (2010).
- <sup>36</sup> White, T. P. and Catchpole, K. R. “Plasmon-enhanced internal photoemission for photovoltaics: Theoretical efficiency limits,”. *Applied Physics Letters* **101**(7), 073905 (2012).
- <sup>37</sup> Seah, M. P. and Dench, W. A. “Quantitative electron spectroscopy of surfaces: A standard data base for electron inelastic mean free paths in solids,”. *Surface and Interface Analysis* **1**(1), 2–11 (1979).
- <sup>38</sup> Chalabi, H., Schoen, D., and Brongersma, M. L. “Hot-electron photodetection with a plasmonic nanostripe antenna,”. *Nano Letters* **14**, 1374 – 1380 (2014).
- <sup>39</sup> Wang, F. and Melosh, N. A. “Plasmonic energy collection through hot carrier extraction,”. *Nano Letters* **11**(12), 5426–5430 (2011).
- <sup>40</sup> Lee, Y. K., Jung, C. H., Park, J., Seo, H., Somorjai, G. A., and Park, J. Y. “Surface plasmon-driven hot electron flow probed with metal-semiconductor nanodiodes,”. *Nano Letters* **11**(10), 4251–4255 (2011).
- <sup>41</sup> Chan, E., Card, H., and Teich, M. C. “Internal photoemission mechanisms at interfaces between Germanium and thin metal films,”. *Quantum Electronics, IEEE Journal of* **16**(3), 373–381 Mar (1980).
- <sup>42</sup> Reineck, P., Lee, G. P., Brick, D., Karg, M., Mulvaney, P., and Bach, U. “A solid-state plasmonic solar cell via metal nanoparticle self-assembly,”. *Advanced Materials* **24**(35), 4750–4755 (2012).
- <sup>43</sup> Wu, K., Chen, J., McBride, J. R., and Lian, T. “Efficient hot-electron transfer by a plasmon-induced interfacial charge-transfer transition,”. *Science* **349**(6248), 632–635 (2015).

**Acknowledgments** This work was performed in part at the Melbourne Centre for Nanofabrication (MCN) in the Victorian Node of the Australian National Fabrication Facility (ANFF). C. N. was supported by an OCE Fellowship from CSIRO. D.E.G. acknowledges the ARC for support through a Future Fellowship (FT140100514) D.E.G. and T.J.D. acknowledge the ANFF for the MCN Technology Fellowships.

**Author contributions** C.N. and S.D. prepared the samples. C.N. performed all the experiments. J.C. and A.R. performed the numerical simulations. All the authors contributed to writing the manuscript.

**Additional information: Supplementary Information** accompanies this paper

**Competing financial interests:** The authors declare no competing financial interests.

## Appendix S1: Additional supporting figures

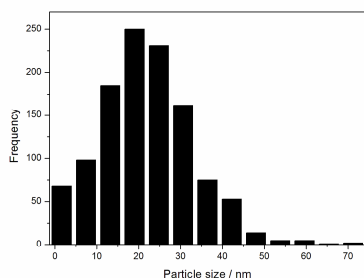
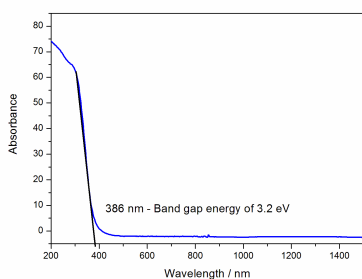
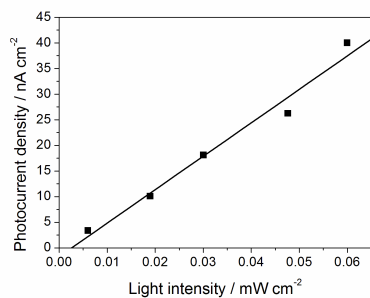
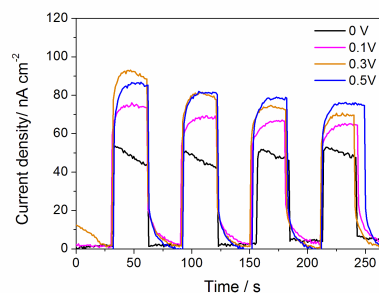
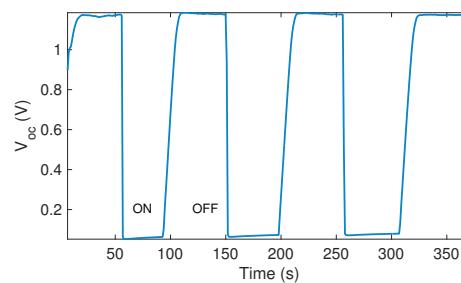


FIG. S1: Measured size distribution of the Au nanoparticles.

FIG. S2: Absorption spectrum of the bare TiO<sub>2</sub> film. Analysis of these data yields a bandgap of 3.2 eV for the material as indicated.FIG. S3: IPCE vs light intensity. Sample: Al/50nmTiO<sub>2</sub>/AuNP Electrolyte: 0.5M Na<sub>2</sub>SO<sub>4</sub> with 20v/v% methanol Wavelength: 600 nm. Bias Voltage: 0.5 VFIG. S4: IPCE vs light intensity. Sample: Al/50nmTiO<sub>2</sub>/AuNP Electrolyte: 0.5M Na<sub>2</sub>SO<sub>4</sub> with 20v/v% methanol Wavelength: 600 nm. Bias Voltage: 0.5 VFIG. S5: Time evolution of the measured open-circuit voltage vs a Ag/AgCl reference electrode. The photo-anode consisted of Au/TiO<sub>2</sub>[50 nm]/Au. Electrolyte: 0.5M Na<sub>2</sub>SO<sub>4</sub> with 20v/v% methanol. Light source 300 W Xenon lamp (Newport Model no. 669092) using a  $\geq 495$  nm cut-off filter (Thorlabs FGL-495).

## Appendix S2: Finite element method (FEM) calculations

The FEM calculations were carried out using COMSOL Multiphysics 5.0, using the model geometry shown in figure S6 (which also shows the the electric field). The model consists of a 500 nm x 500 nm x 2000 nm unit cell, with periodic boundary conditions on the sides and scattering boundary conditions for the top and bottom boundaries. The nanoparticle (AuNP) layer was 14 nm thick, the TiO<sub>2</sub> layer was allowed to have variable thickness and the reflecting mirror had a fixed thickness of 150 nm. The refractive index of Au taken from literature<sup>1</sup>. The AuNP layer thickness was determined by calculating the surface coverage of nanoparticles (47%) from the SEM image shown in the main text and applying volume conservation. A 7 nm solid gold film has the same volume as a 14 nm film with 47% surface coverage, so we take 14 nm as the average height of the nanoparticles. The optical constants of the TiO<sub>2</sub> film were taken from ellipsometry data. Illumination was modelled with a plane wave launched from the top boundary of the simulation geometry.

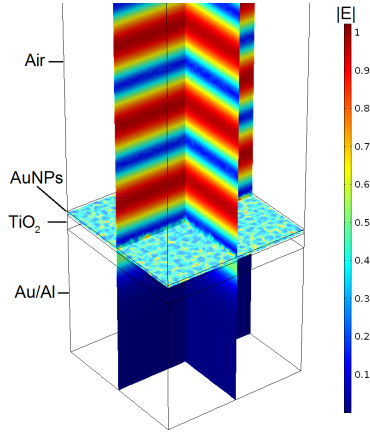


FIG. S6: The FEM model geometry used to calculate the total absorption of the device and the location of the absorption. Here the normalized magnitude of the electric field is shown.

Figure S7 shows the scheme used to calculate the total absorption in the metal/semiconductor/metal structures and the absorption of light by the AuNP film and the reflecting layer. The first step is to convert the measured SEM image to a monochrome bitmap. A function  $f$  is then created whose value at a particular coordinate  $(x, y)$  in the image is 1 if there is gold at that location and 0 otherwise:

$$f(x, y) = \begin{cases} 0 & \text{pixel}(x, y) = \text{black}, \\ 1 & \text{pixel}(x, y) = \text{white}. \end{cases} \quad (\text{S1})$$

With  $f$ , it is possible to define a spatially-dependent relative permittivity:

$$\epsilon(x, y, \lambda) = \epsilon_0 + f(x, y)(\epsilon_{Au}(\lambda) - \epsilon_0). \quad (\text{S2})$$

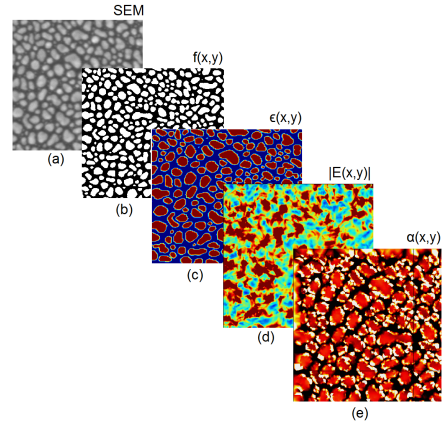


FIG. S7: A scheme for calculating absorption from SEM image. Convert the SEM (a) into a monochrome bitmap (b), then use this to define a material with  $(x, y)$ , a spatially dependent relative permittivity, (c). This material can then be used in FEM calculations to determine the electric field (d) and thus the electromagnetic absorption,  $\alpha$ , in the layer (e).

Figure S8 shows the calculated spatial distribution of electromagnetic fields in samples with and without a metal reflecting layer.

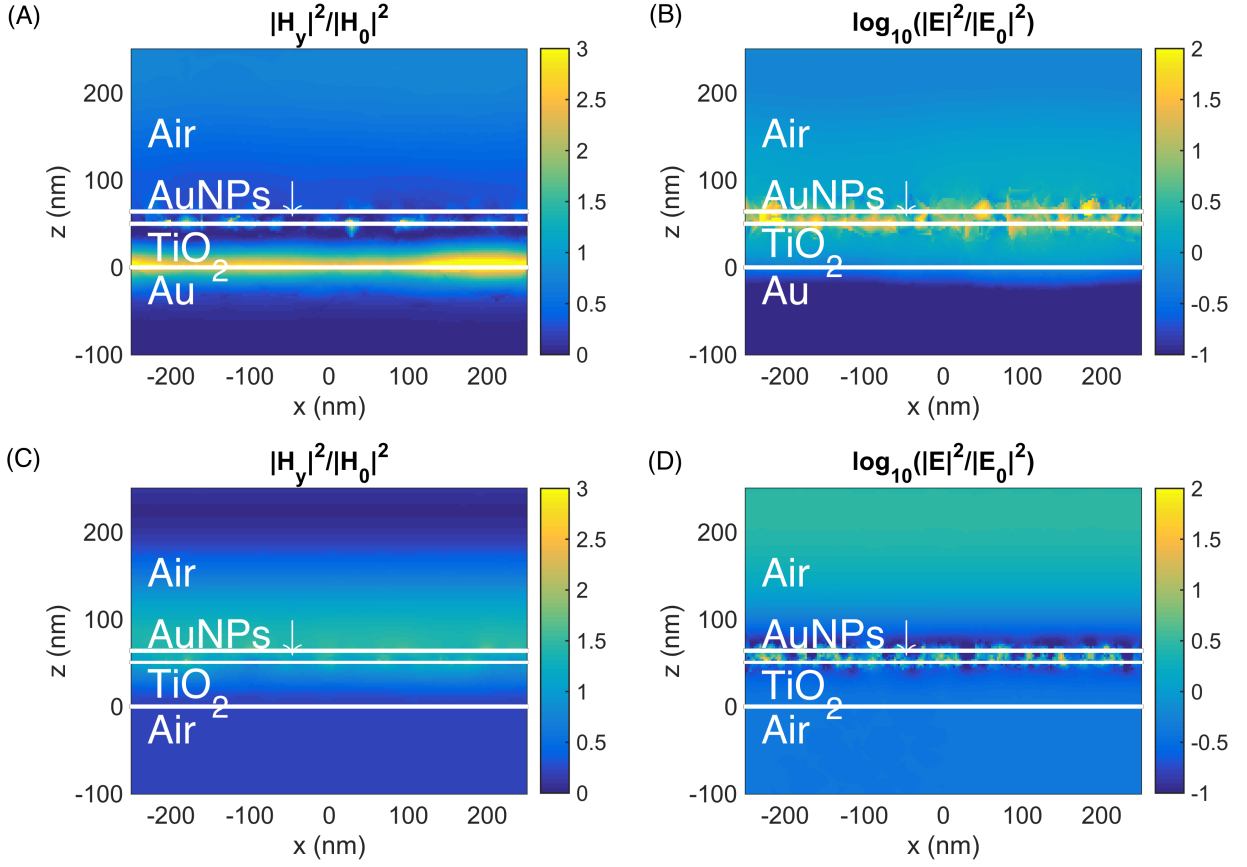


FIG. S8: spatial distribution of electromagnetic fields in samples with (A,B) and without (C,D) a metal reflecting layer for a wavelength of 600 nm.

### Appendix S3: Model of the internal quantum efficiency $\eta$

We consider a top illuminated metal/semiconductor/metal–nanoparticle structure, where the top metal layer consists of metal nanoparticles. This top layer forms a Schottky contact with the semiconductor with a barrier height  $\Phi_{SB}$  (we ignore Fermi pinning effects or any other effects due to surface imperfections), and we describe in this section the electron flow that originates from the nanoparticles (possible thermally activated charge flow on the opposite direction is not considered).

The incident photon–to–electron conversion efficiency is described, to a good level of accuracy, by the product of the absorption efficiency  $A(\lambda)$  of the top layer and the internal quantum efficiency  $\eta(\lambda)$  for detecting a hot charge carrier per each absorbed photon:

$$\text{IPCE}(\lambda) = A(\lambda)\eta(\lambda). \quad (\text{S1})$$

$\eta$  is approximated as the following product:

$$\eta = \eta_{\text{inj}} \times \eta_{\text{trpt}} \times \eta_{\text{inj}m} \times \eta_{\text{ed}}, \quad (\text{S2})$$

where:

- $\eta_{\text{inj}}$ : the injection efficiency of hot electrons into the semiconductor material,
- $\eta_{\text{trpt}}$  the probability that the electron travels through the semiconductor into the second interface,
- $\eta_{\text{inj}m}$  the transmission coefficient for electrons travelling from the semiconductor into the metal electrode/reflector and,
- $\eta_{\text{ed}}$  the efficiency of the redox processes that lead to charge injection from species in solution to positively charged Au nanoparticles.

We now consider each of these processes in detail.

#### .1. $\eta_{\text{inj}}$ : Injection efficiency

The injection efficiency is the probability of photoexcitation of electrons (by way of surface plasmon relaxation) with kinetic energies in excess of the metal–semiconductor Schottky barrier and with sufficient momentum to traverse the barrier. Injection requires a non-vanishing transmission coefficient across the barrier.

##### a. Energy distribution of photo-excited electrons

Illumination of the nanoparticles results in the excitation of surface plasmons. Non–radiative (Landau) dephasing of these excitations leads to the energy transfer from a surface plasmon (with energy  $h\nu$ ) to a single

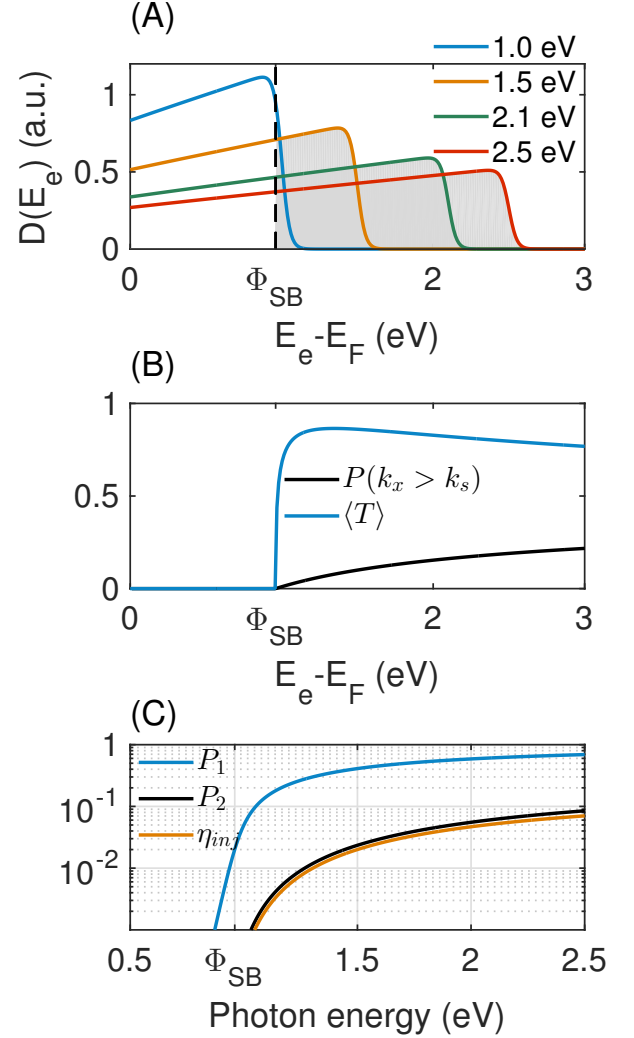


FIG. S9: Injection efficiency. (A) Energy distribution of photo-excited electrons. The horizontal scale represents the excess electron energy with respect to  $E_F$ . The distributions were calculated for different energy values (in eV) of incident photons as indicated in the legend. (B) Fraction of the electron population with momenta within the escape cone ( $P(k_x > k_s)$ ). Transmission coefficient  $\langle T \rangle$  shown as a function of excess electron energy. (C)  $P_1$ : fraction of the electron population with energies above  $\Phi_{SB}$  shown as a function of incident photon energy.  $P_2$ : is the fraction of the electron population with  $E_e > \Phi_{SB}$  and with momenta within the escape cone.  $\eta_{\text{inj}}$  is the injection efficiency which corresponds to  $P_2$  weighted by the transmission coefficient  $\langle T \rangle$ .

electron hole–pair resulting in the excitation of electrons from below the Fermi level of the metal  $E_F$  with energies  $E_F - h\nu < E_i < E_F$  to unoccupied states with energies  $E_F + E_e$  with  $E_e$  being the excess kinetic energy of the electron where  $0 < E_e < h\nu$ . The energy distribution of these excited states has been argued to be almost uniform due to the fact that Landau damping occurs as intraband transitions between states of  $sp$  character that have constant energy–densities a few eV above and below

the  $E_F$  for metals<sup>2</sup>.

Here, we take the approach described by White and Catchpole<sup>3</sup> to estimate the shape of the hot-electron energy density distribution  $D(E_e; h\nu)$ :

$$D(E_e; h\nu) \propto \rho(E_e - h\nu) f(E_e - h\nu) \rho(E_e) [1 - f(E_e)], \quad (\text{S3})$$

where  $\rho(x)$  is well approximated by the free-electron gas model,  $\rho(x) \sim x^{1/2}$  and  $f(x)$  is the Fermi-Dirac distribution function. This approximation does not take into account the conservation of momentum in the electronic transitions. The shape of this distribution is shown in figure S9(A) for four values of incident photon energy, assuming a metal work function of 5.1 eV and a Schottky barrier height of 1 eV. The shaded area in these curves correspond to the fraction of the resulting population with energies above the Schottky barrier, a fraction shown *vs*  $h\nu$  by curve  $P_1$  in figure S9(C).

#### b. Escape cone in momentum space

Let us consider the metal-semiconductor interface as consisting of an infinite plane in space. If we represent with  $x$  the axis normal to the interface, then a requirement for electron injection is that the  $x$  component of the electron momentum  $k_{sx} = k_e \cos(\Omega_s)$  should have an associated energy larger than the Schottky barrier. This condition allows us to define an escape cone of angle  $\Omega_s$  in  $k$  space by:

$$k_{sx} = k_e \cos(\Omega_s) = \sqrt{2m\Phi_{SB}/\hbar}. \quad (\text{S4})$$

The fraction of the hot-electron population that possesses  $x$  components of their momentum with an associated kinetic energy with sufficient magnitude to cross the interface, is given by the ratio of the solid angle subtended by  $\Omega_s$  to the solid angle of the entire sphere of constant energy in  $k$  space (under the assumption of uniform distribution of momenta):

$$\begin{aligned} P(k_x > k_s) &= \frac{1}{4\pi} \int_0^{2\pi} \int_0^{\Omega_s} \sin(\theta) d\theta d\phi \\ &= \frac{1}{2} [1 - \cos(\Omega_s)] \\ &= \frac{1}{2} \left( 1 - \sqrt{\frac{\Phi_{SB}}{E_e}} \right), \end{aligned} \quad (\text{S5})$$

valid for  $E_e > \Phi_{SB}$ . This result shows that the fraction of hot-electrons moving to the flat metal-semiconductor interface asymptotes to 1/2 for the cases where  $\Phi_{SB} \rightarrow 0$  or  $E_e \gg \Phi_{SB}$ . Figure S9(B) shows how this fraction of the hot-electron population varies with electron energy, whereas figure S9(C) shows the fraction of the population that meets both the energy and momentum requirements for electron injection (curve  $P_2$ ).

When  $D(E_e; h\nu)$  is an uniform distribution, it can be shown that the fraction of the hot-electron population

that has both the energy and momentum required for electron escape:

$$\int_{\Phi_{SB}}^{\infty} D(E; h\nu) P(k_x > k_s),$$

asymptotes to the Fowler equation<sup>4</sup>.

#### c. Transmission coefficient

One more consideration to bear in mind is the possibility of reflections at the metal-semiconductor interface, which arises due to the possible mismatch between the momenta of the hot-electron in both media. On the metal side, the kinetic energy of the hot-electron is:

$$E_k = E_e = \frac{\hbar^2}{2m_e} [k^2], \quad (\text{S6})$$

whereas on the semiconductor side it becomes

$$E_e - \Phi_{SB} = \frac{\hbar^2}{2m_e^*} (\kappa^2), \quad (\text{S7})$$

where in general  $m_e \neq m_e^*$ . The transmission coefficient  $T$  at the interface is given by:<sup>5</sup>

$$\begin{aligned} T &= \frac{4k_{sx}\kappa_x}{m_e m_e^* (k_{sx}/m_e + \kappa_x/m_e^*)^2} \\ &= \frac{4k_{sx}\kappa \cos(\theta)}{m_e m_e^* (k_{sx}/m_e + \kappa \cos(\theta)/m_e^*)^2}, \end{aligned} \quad (\text{S8})$$

where  $k_{sx}$  is given by Eqn. (S4) and we have considered only those hot-electrons within the escape cone subtended by  $\Omega_s$ .  $T$  has been written in terms of the total momentum  $\kappa$  inside the semiconductor and the angle  $\theta$  of its projection on the axis perpendicular to the interface (i.e.  $\kappa_x = \kappa \cos(\theta)$ ).

In the work of Chalabi *et al*<sup>6</sup> it was assumed that due to the translation invariance of their metal-semiconductor interface along one direction, the momentum component parallel to the interface  $k_y$  was conserved during the charge transfer process. This condition simplifies the calculation of the transmission probability of eqn. (S8), but it is a condition that may not be satisfied in general (e.g. for metal nanoparticles). A more general consideration consists on assuming conservation of the total momentum and accounting for possible changes in the direction of the momentum after injection: the electrons move away from the metal, or equivalently that the angle  $\theta$  on eqn. (S8) varies from 0 to  $\pi/2$ . With this in mind, an angle-averaged transmission coefficient  $\langle T \rangle$  can be calculated as follows:

$$\begin{aligned} \langle T \rangle &= \frac{1}{2\pi} \int_0^{2\pi} \int_0^{\pi/2} \frac{4\alpha \cos(\theta)}{(\alpha + \cos(\theta))^2} d\phi d\theta \\ &= 4\alpha \left[ \ln \left( \frac{\alpha + 1}{\alpha} \right) + \frac{\alpha}{1 + \alpha} - 1 \right], \end{aligned} \quad (\text{S9})$$

where  $\alpha = k_{sx}m_e^*/\kappa m_e = \sqrt{\frac{m_e^*\phi_b}{m_e(E_e - \Phi_{SB})}}$ . This transmission coefficient is shown in figure S9(B)  $\langle T \rangle$  assuming an Au–TiO<sub>2</sub> interface and a ratio for electron effective mass of 0.0862 (data taken from Zhang *et al*<sup>7</sup>). Similar results are reported by Nienhaus *et al*<sup>8</sup>.

The efficiency of hot–electron injection  $\eta_{inj}$  is then calculated as:

$$\eta_{inj}(h\nu) = \frac{\int_{\phi_b}^{\infty} dE D(E; h\nu) P(k_x > k_s) \langle T(E) \rangle}{\int_0^{\infty} dE D(E; h\nu)}. \quad (S10)$$

$\eta_{inj}$  depends on the height of the Schottky barrier height  $\Phi_{SB}$ , the incident photon energy  $h\nu$ , the ratio of electron effective masses in the metal and semiconductor material and the temperature. Figure S9(C) shows  $\eta_{inj}$ .

### .2. $\eta_{trpt}$ : Transport efficiency

This is the probability that an electron entering the semiconductor layer (of thickness  $t$ ) traverses it without experiencing a scattering event (such as trapping at defect sites). This depends on the mean free path of charge carriers on the semiconductor material  $l_{eff}(E_e)$ , which, in turn, depends on the excess energy of the electron  $E_e$ :

$$\eta_{trpt}(E_e) = \frac{1}{t} \int_0^t \exp(-z/l_{eff}(E_e)) dz. \quad (S11)$$

The mean free path for electrons in TiO<sub>2</sub> was obtained at each electron energy from the universal curve compiled in reference<sup>9</sup>. For a thickness of 50 nm, the transport efficiency is shown in figure S10(A), which clearly shows that high energy electrons experience more scattering.

### .3. $\eta_{inj}$ : Injection into metal reflector/mirror

This last step is dictated by the electron transmission probability at this final interface  $\langle T_{bottom} \rangle$ , which can be calculated in an analogous manner to what was described previously. Following this rationale, the angle–averaged transmission coefficient is given by:

$$\eta_{inj} = \frac{\langle T_{bottom} \rangle}{\frac{(2\beta^2 + 2) \ln(\beta + 1) - 2\beta^2 \ln(\beta) - 2\beta}{\beta}}, \quad (S12)$$

where:

$$\beta^2 = \frac{m(E_e - \Phi_{SB})}{m^*(E_e - \Phi_{SB} - eV)}. \quad (S13)$$

where  $eV$  is the magnitude of the applied bias across the MSM junction. The magnitude of this transmission coefficient is shown in figure S10(A) ( $\langle T_{bottom} \rangle$ ).

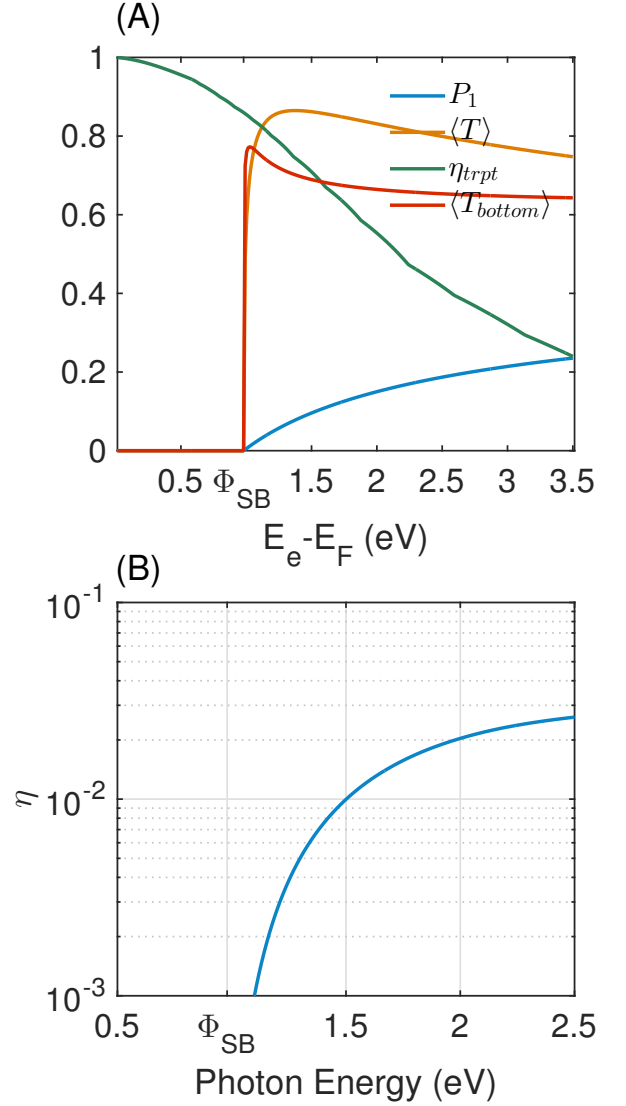


FIG. S10: Internal quantum efficiency. (A) Plots of  $\eta_{trpt}$  and  $\eta_{inj}$  shown as a function of electron excess energy above the metal’s Fermi level ( $E_F$ , in eV). For comparison, we also reproduce the curves  $P_1$  and  $\langle T \rangle$  of figure S10. (B)  $\eta$  vs incident photon energy for  $\Phi_{SB}=0.98$  eV

The internal quantum efficiency  $\eta$  is then calculated, as a function of incident photon energy as:

$$\eta(h\nu) = \frac{\int_{\phi_b}^{\infty} D(x; h\nu) P(k_x > k_s) \langle T(x) \rangle \eta_{trpt}(x) \langle T_{bottom}(x) \rangle dx}{\int_0^{\infty} dE D(x; h\nu)}.$$

$\eta$  is shown in figure S10(B). Figure S11 shows the expected effect of  $\Phi_{SB}$  and semiconductor thickness on  $\eta$ . Similar lineshapes have been obtained by Leenheer *et al*<sup>10</sup>

This model is expected to largely overestimate the IPCE at shorter wavelengths due to the fact that no attempt was made to consider possible photocurrent con-

tributions due to the excitation of surface plasmon polaritons at the Au mirror/TiO<sub>2</sub> interface. As discussed in the main text and by Chalabi *et al*<sup>6</sup> and Wang and Melosh<sup>11</sup>, these currents will have an opposite sign to the ones produced by photoexcitation and plasmon decay by the metal nanoparticles.

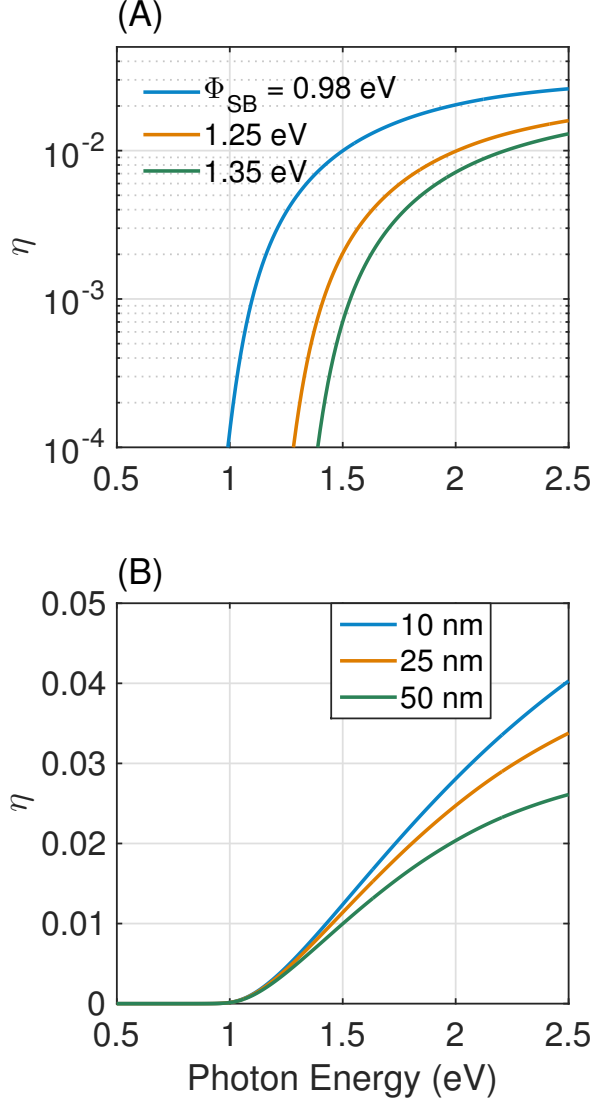


FIG. S11: Effect of Schottky barrier height (A) and semiconductor thickness (B) on  $\eta$

- 
- \* Electronic address: charlene.ng@csiro.au
- † Electronic address: daniel.gomez@csiro.au
- <sup>1</sup> Palik, E., editor. *Handbook of Optical Constants of Solids*. Academic Press, (1985).
- <sup>2</sup> Moskovits, M. “Surface-enhanced spectroscopy,”. *Rev. Mod. Phys.* **57**(3), 783–826 Jul (1985).
- <sup>3</sup> White, T. P. and Catchpole, K. R. “Plasmon-enhanced internal photoemission for photovoltaics: Theoretical efficiency limits,”. *Applied Physics Letters* **101**(7), 073905 (2012).
- <sup>4</sup> Scales, C. and Berini, P. “Thin-film schottky barrier photodetector models,”. *Quantum Electronics, IEEE Journal of* **46**(5), 633–643 May (2010).
- <sup>5</sup> Davies, J. H. *The Physics of Low-dimensional Semiconductors: An Introduction*. Cambridge University Press, (1998).
- <sup>6</sup> Chalabi, H., Schoen, D., and Brongersma, M. L. “Hot-electron photodetection with a plasmonic nanostripe antenna,”. *Nano Letters* **14**, 1374 – 1380 (2014).
- <sup>7</sup> Zhang, J., Zhou, P., Liu, J., and Yu, J. “New understanding of the difference of photocatalytic activity among anatase, rutile and brookite TiO<sub>2</sub>,”. *Phys. Chem. Chem. Phys.* **16**, 20382–20386 (2014).
- <sup>8</sup> Nienhaus, H., Gergen, B., Weinberg, W., and McFarland, E. “Detection of chemically induced hot charge carriers with ultrathin metal film schottky contacts,”. *Surface Science* **514**(1–3), 172 – 181 (2002).
- <sup>9</sup> Seah, M. P. and Dench, W. A. “Quantitative electron spectroscopy of surfaces: A standard data base for electron inelastic mean free paths in solids,”. *Surface and Interface Analysis* **1**(1), 2–11 (1979).
- <sup>10</sup> Leenheer, A. J., Narang, P., Lewis, N. S., and Atwater, H. A. “Solar energy conversion via hot electron internal photoemission in metallic nanostructures: Efficiency estimates,”. *Journal of Applied Physics* **115**(13), – (2014).
- <sup>11</sup> Wang, F. and Melosh, N. A. “Plasmonic energy collection through hot carrier extraction,”. *Nano Letters* **11**(12), 5426–5430 (2011).